

A comparative study of surface layer formation in Ni-based alloys with varying Cr contents exposed to high temperature fluoride environment

Rumu H. Banerjee ^{a, b, *}, Vishal Singh ^a, A. Arya ^{a, b}, S. Banerjee ^b

^a Materials Science Division, Bhabha Atomic Research Centre, Mumbai, 400 085, India

^b Homi Bhabha National Institute, Mumbai, 400 085, India

HIGHLIGHTS

- Ni-based alloys exposed to molten FLiNaK salt under air atmosphere develop patches of mixed oxides at surface.
- Alloy 690 and Alloy 693 developed mixed oxide layers of the types NiO + Cr₂O₃ and NiO + Al₂O₃ + Cr₂O₃, respectively.
- These oxides formed galvanic micro-couples with exposed alloy surface leading to increase in Cr depletion from the alloy.
- Ni-17 wt.% Mo-7wt.% Cr alloy formed MoO₃ + NiO + Cr₂O₃ type mixed oxide layer.
- A thin MoO₃ layer present on the exposed alloy surface reduces the effect of galvanic coupling thereby lowering Cr depletion.

ARTICLE INFO

Article history:

Received 1 July 2018

Received in revised form

12 November 2018

Accepted 1 January 2019

Available online 2 January 2019

Keywords:

Ni-based alloys

Molten salt interaction

Surface film

ABSTRACT

Microstructural and surface characterization of Ni-based alloys viz. Alloy 690, Alloy 693 and Ni-17 wt.% Mo- 7wt.% Cr exposed to molten FLiNaK salt under air atmosphere at 973 K was carried out. Patches of mixed oxide layers of type NiO + Cr₂O₃, NiO + Al₂O₃ + Cr₂O₃ and MoO₃ + NiO + Cr₂O₃ were observed for Alloy 690, alloy 693 and Ni-Mo-Cr alloy, respectively. Corrosion susceptibility index and calculated Cr diffusivity in the alloys followed the order: Alloy 690 > Alloy 693 > Ni-Cr-Mo alloy. The oxide layers developed are only partially protective as they form a galvanic micro-couple with exposed surface which makes the later more prone to attack. The lower Cr depletion in case of Ni-Mo-Cr alloy as compared to Alloy 690 and 693 can be attributed to the fact that MoO₃ layer is formed over the areas devoid of oxide patches which may prevent/reduce galvanic coupling between Ni-,Cr-rich oxides and exposed surface.

© 2019 Elsevier B.V. All rights reserved.

1. Introduction

Molten fluoride salts are excellent candidates for various advanced technological applications such as fuel/coolant in advanced nuclear reactors, thermal energy storage from solar power, chemical production plants etc [1–3]. These fluoride salts offer advantages over other salts in terms of good thermal conductivity, chemical inertness, high boiling point, large specific heat and low vapour pressure [4,5]. However, use of molten fluoride salts in such applications, especially in prospective fast and epithermal molten salt reactors (MSR) pose a great challenge mainly in terms of its

compatibility with the structural materials [6]. For MSR both fuel and coolant are fluoride melts and thus corrosion resistance of the structural component at high temperature and chemically aggressive environment becomes a major issue which needs to be investigated.

Materials corrosion induced by fluoride melts occur mainly via thermodynamically driven selective dissolution of elements into the melts [6,7] and hence the alloying elements are primarily selected based on the Gibbs free energy of formation of their fluorides [6,7]. The dissolution tendency of different metals in fluoride melt increases in the following order: W < Mo < Ni < Co < Fe < Cr < Al < Na and is mainly diffusion controlled [2]. Presence of moisture, HF and high valency ions such as Cr³⁺ in molten salt are observed to aggravate localized corrosion in the form of pits and inter-granular attack by accelerating dissolution of Cr [7,8]. Similarly galvanic couple formation by the elements in molten salt and structural alloy

* Corresponding author. Materials Science Division, Bhabha Atomic Research Centre, Mumbai, 400 085, India.

E-mail address: rumuhalder24feb@gmail.com (R.H. Banerjee).

also affect the corrosion rate and alloy microstructure [8]. In such harsh conditions, Ni-based superalloys are often considered for use owing to their high temperature strength and stability as well as resistance against corrosive and radiative environment [9,10]. The ability of any material to withstand the severe corrosive environment mainly depends on the formation and stability of protective surface films and their diffusion barrier characteristics against the outward diffusion of the constituent elements from the alloy matrix [11]. In general, addition of elements such as Al, Cr etc. in the structural alloy promote formation of alumina or chromia depending on their concentration in the alloy and presence of oxygen environment. Though Cr and Al are prone to selective attack, they are added in various Ni-based alloys mainly to impart oxidation resistance [9–11].

Presence of oxygen in molten fluoride as an impurity or due to accidental ingress, can alter the corrosion mechanism by facilitating the formation of surface films. Available studies carried out on compatibility of different alloys like GH3535 alloy, stainless steel 316 and Hastelloy N with molten fluoride salt mainly address Cr dissolution in fluoride melt [12–17]. However no results are available on characteristics of surface films which form on the structural alloys under the conditions of accidental oxygen ingress. It is therefore necessary to characterize the surface films which can form in fluoride melt in presence of oxygen.

The main aim of this study is to characterize the surface film formation on Ni-based alloys with varying Cr contents in fluoride melt in presence of oxygen and investigate their role in enhancing or prohibiting the migration of various elements migrating from alloy to melt, and vice-versa. Such study is important since alloys with different Cr contents will form different surface films which can have different stability towards fluoride attack. The Ni-based alloys chosen for present investigation are Alloy 690, Alloy 693 which are both considered for vitrification melter pot applications [18–21] as well as Ni-Mo-Cr alloy, a candidate material considered for the initial molten salt reactor experiment (MSRE) in Oak Ridge National Laboratory (ORNL) [2].

2. Experimental

2.1. Materials

Coupons of Alloy 690, Alloy 693 and the Ni-Mo-Cr alloy (compositions in Table 1) having dimensions 1 cm x 1 cm x 1 mm were taken. The specimen surface was made scratch free and polished upto mirror finish using standard metallographic techniques for obtaining accurate post interaction analyses. Alloy 690 and 693 were used in as received mill-annealed condition while Ni-Mo-Cr alloy was given a solution annealing treatment at 1177 K for 1 h followed by water quenching. Analytical grade LiF, NaF and KF salts were taken in ratio of 46.5–11.5–42 mol% (eutectic composition; FLiNaK salt) respectively, mixed thoroughly and then vacuum dried at 393 K following the procedure mentioned by Ouyang et al. [8]. The residual moisture following this procedure is normally 1.9–3.2 wt.%. The salt was immediately transferred onto an alumina crucible containing the alloy coupons. The crucible was then placed

in a furnace maintained at 973 K and held at the same temperature for 3 h followed by furnace cooling. The experiment was carried out at ambient atmosphere to simulate the effect of accidental service conditions and facilitate oxide layer formation. The time period for interaction between alloy and fluoride melt is small and is so chosen since the impurity driven corrosion (HF, oxide, other ions) is dominant at short durations [2,8]. The exposed samples were washed with 1 mol/L solution of aluminium nitrate and subsequently cleaned ultrasonically using acetone and de-ionized water to remove excess salts and the metal fluorides at the alloy surface [2,8,10].

Analysis of morphology and microstructure of the exposed coupons were carried out using a Scanning Electron Microscope (Carl Zeiss Auriga CrossBeam) equipped with energy dispersive spectroscopy (EDS). Secondary electron (SE) imaging was used to observe the surface morphology while back scattered electron (BSE) mode imaging was used to observe the Z-contrast. Subsequent quantitative measurements using X-rays were recorded using a focused electron beam accelerated to 20 kV. The X-ray diffraction measurements on the exposed samples were recorded using Bruker D8 Discover X-ray diffractometer using Cu K α radiation source ($\lambda = 1.5406 \text{ \AA}$) in a range $30^\circ - 70^\circ (2\theta)$ with step size of 0.02° .

The surface films developed on the alloys were characterised using X-ray photo electron Spectroscopy (XPS). The XPS measurements were carried out at a base pressure of $<1 \times 10^{-9}$ mbar using monochromatic beam of Al K α ($h\nu = 1486.74 \text{ eV}$) X-rays. A survey scan was taken in the binding energy range from 0 to 1000 eV to identify the major elements present at the surface. High resolution energy spectra were then recorded for Ni 2p, Al 2p, Cr 2p, Fe 2p, Mo 3d and O 1s followed by necessary baseline, binding energy and flood gun corrections. All the measurements were carried out at pass energy of 11 eV. The instrumental resolution was 0.5 eV and all the energies were referenced wrt C 1s peak occurring at 284.6 eV. The XPS peaks were deconvoluted and fitted by a Voigt line profile with 30% Lorentzian component. Quantitative analysis was carried out using CASA-XPS software employing Shirley background.

3. Results

3.1. Microstructural studies on alloys

The microstructure of solution annealed Ni-Mo-Cr alloy is found to be devoid of any precipitates containing only equi-axed grains (Fig. 1(a)). After exposure to FLiNaK melt, patches of oxide layer was formed on alloy surfaces. Alloy surface devoid of oxide patch showed formation of pits (depleted in Cr) and grain boundary attack (Fig. 1(b)) owing to selective dissolution of Cr into melt which is consistent with the previous observations made on Hastelloy B3, N etc. [2,8,10]. This selective depletion of Cr from various alloys under fluoride attack is attributable to negative Gibbs free energy of formation of Cr-fluoride [8]. The observed pits are mainly attributed to the coalescence of vacancies generated by outward diffusion of Cr through lattice diffusion while Cr diffusion through the high energy grain boundary result- in grain boundary attack [22]. SE, BSE imaging and detailed X-ray mapping of the alloy cross-section before and after exposure indicate formation of an oxide layer rich in Ni and Cr ($\sim 3 \mu\text{m}$) followed by a Cr depleted and pitted region ($\sim 6 \mu\text{m}$) (Fig. 2(a)–(c)). Additionally, irregularly shaped Mo rich precipitates were observed below the Cr depleted region (Fig. 2(c)). EDS analysis suggest that these precipitates are Mo₂C type carbides and are thermodynamically favoured at this temperature as they have a Gibbs free energy of $\sim -54.55 \text{ kJ/mol}$ [14].

The as-received microstructure of Alloy 693 has clusters of Cr₂₃C₆ type precipitates along the grain boundaries and isolated

Table 1
Composition of Alloy 690, Alloy 693 and Ni-Mo-Cr alloy used in present study calculated from EDS and XRF analyses.

Alloy/Wt.%	Ni	Cr	Mo	Fe	Al	Others
Ni-Mo-Cr alloy	77	7	16			
Alloy 693	Balance	29.2	—	3.96	3.19	Nb: 1.86 Ti: 0.42
Alloy 690	Balance	30.8	—	10.3	<0.50	Cu + Mn < 1.0

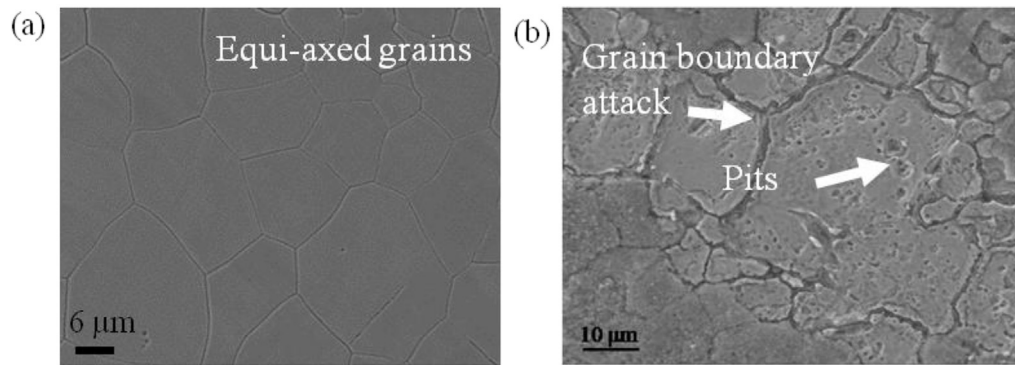


Fig. 1. (a) Microstructure of solution annealed Ni-Cr-Mo alloy and (b) Exposed surface of Ni-Mo-Cr alloy showing formation of pits within grain along with the X-ray maps for Ni K α , Cr K α , Mo K α and O K α , showing Cr and O enrichment along grain boundary.

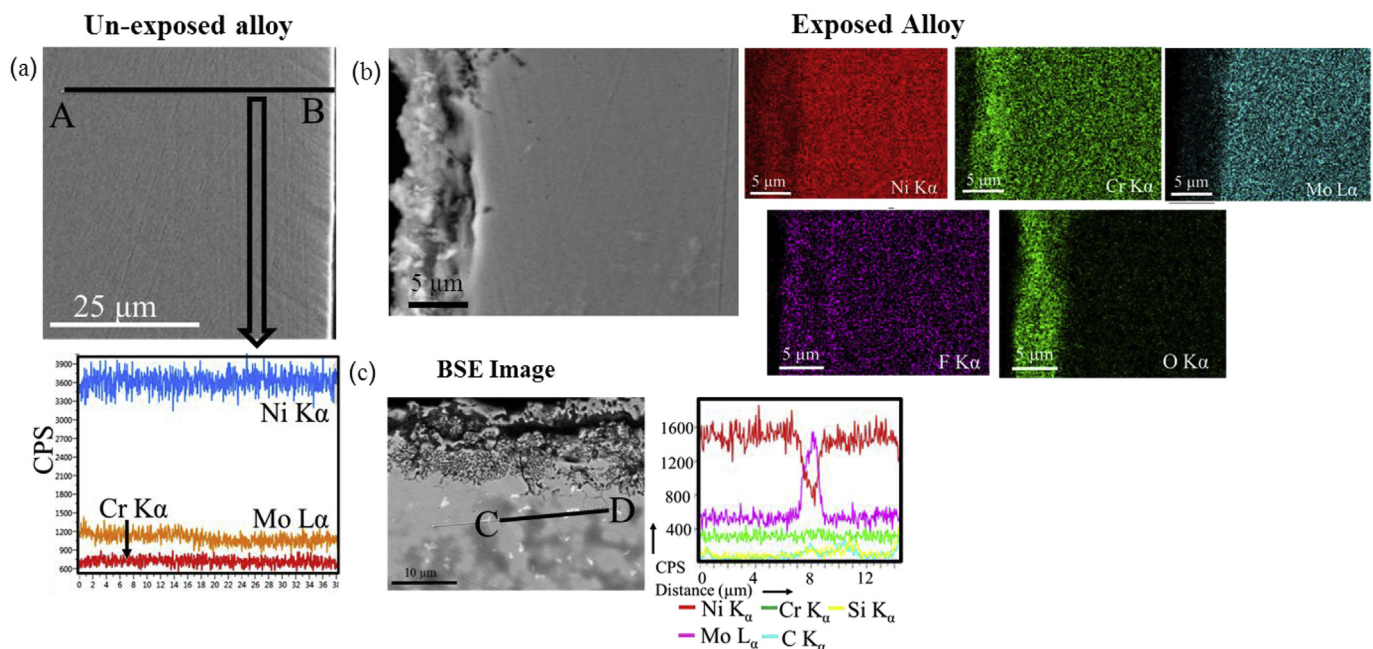


Fig. 2. (a) SE image and EDS line scan along the cross section of un exposed Ni-Mo-Cr alloy and (b) SE image and cross sectional X-ray maps of Ni K α , Cr K α , F K α , O K α and Mo L α showing formation of Ni and Cr rich oxide at surface in Ni-Mo-Cr alloy. (c) BSE image and EDS line scan of the alloy cross-section after exposure to molten salt showing formation of Mo-rich carbides.

blocky precipitates of NbC (Fig. 3(a)). Detailed micro-structural aspects of Alloy 693 are discussed elsewhere [19,21]. Alloy 693 also showed formation of a black surface layer in patches after exposure to FLiNaK melt. SE imaging and X-ray mapping of the alloy surface and cross-section (Fig. 4) show that the surface layer formed is rich in O, Cr and Al (~2 μm). The Al rich type surface oxide developed all over the alloy surface but remained depleted in grain boundaries. This suggests that the grain boundary diffusion mechanism is responsible for dissolution of Al into the melt in case of Alloy 693 [23]. The oxide layer is followed by an Al and F (~2 μm) enriched layer. Adjacent to this layer, a Cr depleted and F enriched region (~8 μm width) containing pits was observed attributable to selective removal of Cr from the alloy and subsequent coalescence of vacancies to form voids/pitted structure [8].

Alloy 690 microstructure mainly comprises an austenitic matrix with equi-axed grains, randomly distributed isolated precipitates of Ti(C, N) and Cr rich Cr₂₃C₆ type carbides which are mainly present at the grain boundaries (Fig. 5 (a)). Detailed microstructural and surface characterization of as received Alloy 690 are presented

elsewhere [20]. In both Alloy 690 and 693, Cr rich carbides of type Cr₂₃C₆ were observed especially along the grain boundaries. The Gibbs free energy of formation for these precipitates is observed to be ~ -389.9 kJ/mol [24]. Thus with increase in Cr content in the Ni matrix formation of grain boundary Cr-rich carbides is facilitated. After exposure, the alloy developed patches of oxide layer rich in Cr while the surface devoid of oxide layer showed intensive grain boundary attack as well as pit formation within the grain attributable to Cr dissolution (Fig. 5(b)). Detailed EDS analyses and X-ray maps for the alloy cross-section reveal formation of Cr-oxide (~4 μm) at surface followed by followed by a pitted region depleted in Cr and enriched in F (~12 μm width) (Fig. 5(c)).

From the microstructural characterization, it is evident that all the three alloys undergo intergranular attack and pit formation owing to selective dissolution of Cr. The depth of Cr depletion is observed to be least for Ni-Mo-Cr alloy and maximum for Alloy 690. Analysis of the salt show that Cr concentration is highest for the salt interacted with Alloy 690 while lowest Cr content was found in the salt interacted with Ni-Mo-Cr alloy. The quantitative elemental analysis for

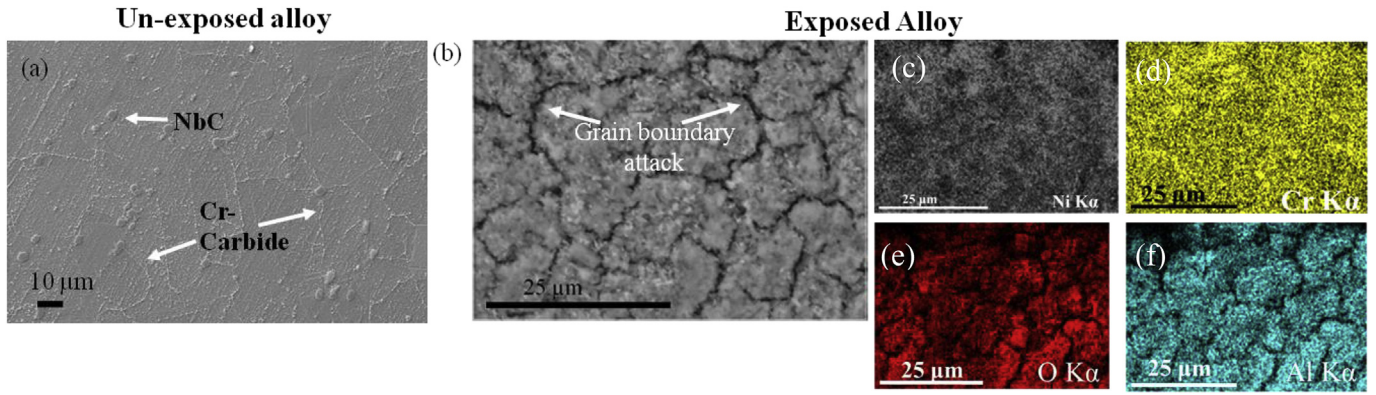


Fig. 3. Surface Morphology of Alloy 693 (a) before exposure and (b) after exposure to molten salt. (c)–(f) The elemental X-ray mapping of Ni Kα, Cr Kα, O Kα and Al for exposed alloy.

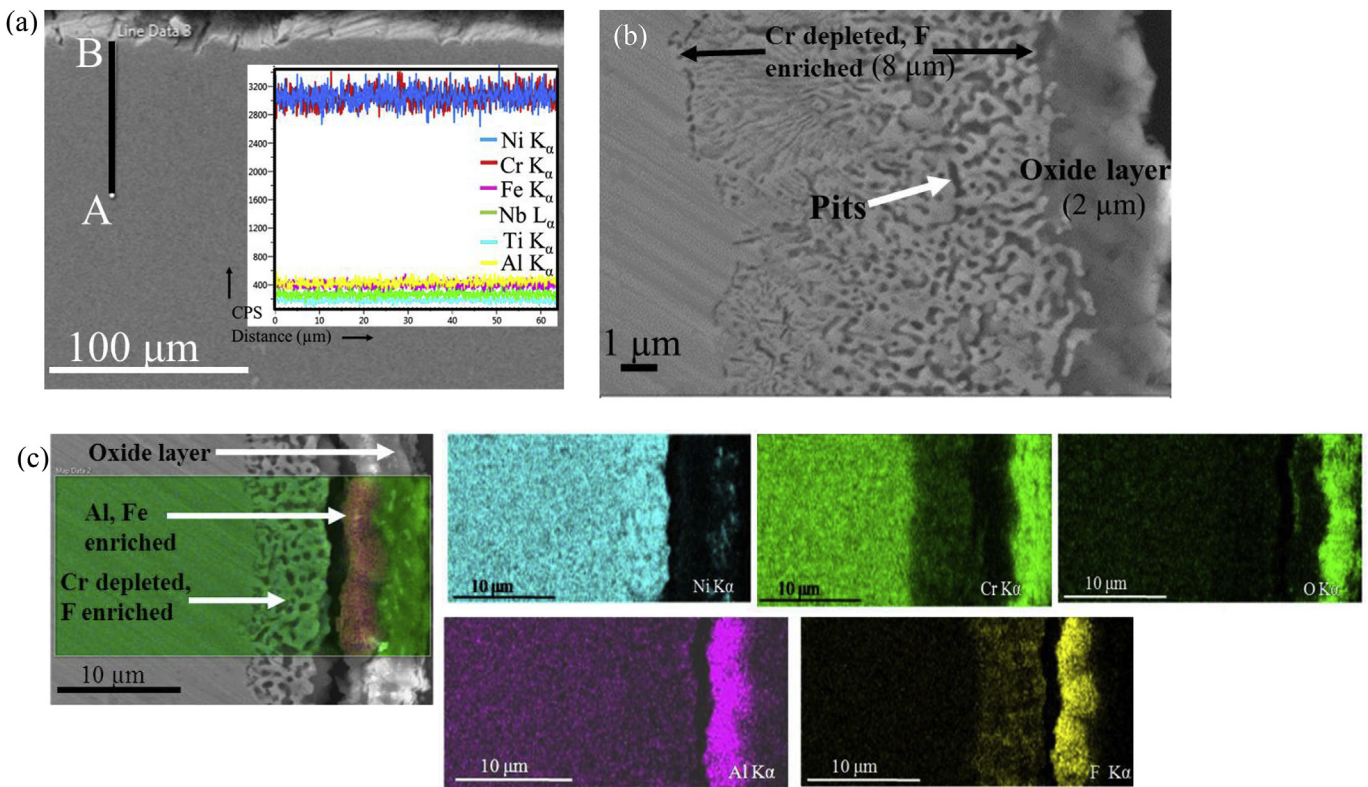


Fig. 4. (a)–(b) Cross sectional SE image of unexposed and exposed Alloy 693 respectively. (c) Cross sectional SE image and corresponding elemental X-ray maps (Ni Kα, Cr Kα, O Kα, Al Kα and F Kα) of exposed coupon of Alloy.693.

pre- and post-interacted FLiNaK salt is given in Table 2. The corrosion susceptibility of these alloys to molten salt corrosion was assessed by quantity W_{Fe+Cr} (wt%) [25]. W_{Fe+Cr} (wt%) was found to show the trend $W_{Fe+Cr}^{Ni-Mo-Cr(7\text{ wt}\%)} < W_{Fe+Cr}^{693}(33\%) < W_{Fe+Cr}^{690}(38\%)$ in consistency with the observed trend in Cr depletion.

3.2. Surface layer characterization using XRD and XPS

XRD analysis of the post-corroded Ni-Mo-Cr alloy indicates formation of mixed oxide of type NiO and Cr_2O_3 (Fig. 6(a)) consistent with SEM-EDS results. XPS measurements carried out on area devoid of macroscopic oxide patch show that Ni exists in Ni^0 and Ni^{2+} state having peak binding energies at 852.5 eV and 858.5 eV respectively (Fig. 6(b)) [11]. For molybdenum, peaks corresponding

to $3d_{5/2}$ and $3d_{3/2}$ were recorded at 232.0 eV and 235.1 eV respectively which correspond to Mo in +6 oxidation state [26]. O 1s peak has been deconvoluted at 528.3 eV and 529.9 eV indicating its presence as oxides of nickel and molybdenum mainly as NiO and MoO_3 (Fig. 6(c) and (d)). Semi-quantitative analyses using CASA XPS reveal that contribution to O 1s peak from the oxygen in MoO_3 is higher (69.54%) as compared to the O is from NiO (30.46%). Presence of metallic state of Ni and Cr along with MoO_3 and NiO suggest that these oxides are either porous or dis-continuous exposing metallic islands at places (Fig. 6(e)).

For Alloy 693, XRD analysis confirms that the surface layer is predominantly Cr_2O_3 and Al_2O_3 type consistent with the SEM observations (Fig. 7(a)). XPS measurements show that the layers devoid of oxide patches had no surface layers over them and the

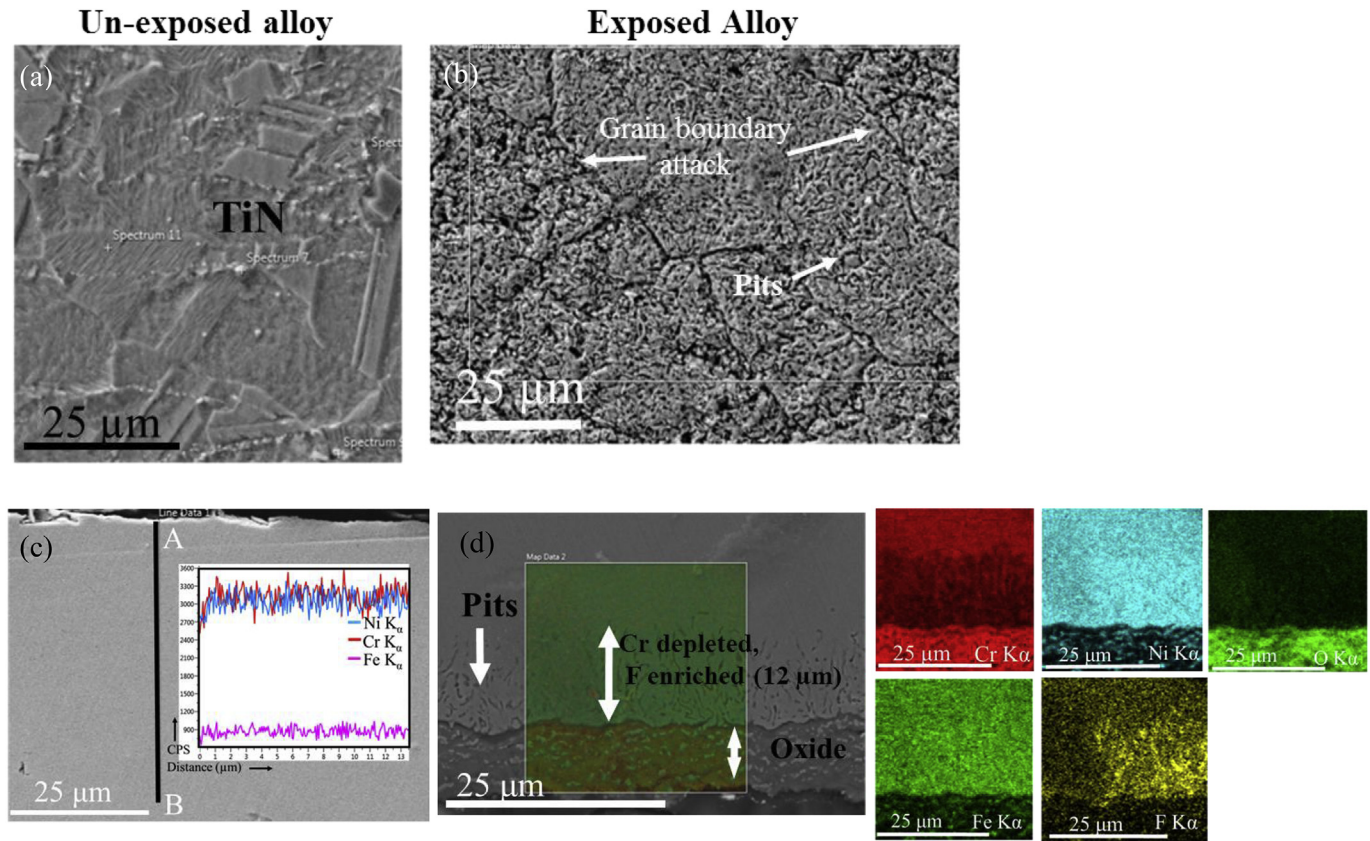


Fig. 5. Surface morphology of Alloy 690 (a) before and (b) after exposure to FLiNaK melt, (c) SEM image along with EDS scan of un-exposed Alloy 690 cross-section and (d) Cross-sectional microstructure and X-ray maps of different elements in Alloy 690 after exposure FLiNaK melt.

Table 2
Molten salt before and after corrosion.

Molten salt	Al (%)	Cr (ppm)	Fe (%)	Mo (ppm)	Ni (ppm)
LiF-NaF-KF mixture	—	47	0.10	8	<5
Salt-reacted with alloy 690	4.97	72	0.24	57	<5
Salt-reacted with alloy 693	3.37	67	67 ppm	6	<5
Salt-reacted with alloy Ni-Mo-Cr	3.14	40	0.13	56	<5

elements were mostly present in their metallic states while the regions with oxide patches reveal formation of mixed oxides. From the XPS analysis of the oxide patch, Ni and Al were observed to be mainly in their +2 and +3 states, respectively. The O1s binding energy peak on deconvolution shows peak positions at 528.4 eV (corresponding to oxide of Ni) and 530.6 eV (corresponding to oxide of Al) indicating that the surface film comprises of oxides of Ni and Al mainly Al_2O_3 and NiO (Fig. 7) [11,27]. Furthermore, contribution to O 1s peak from the oxygen in Al_2O_3 is higher (73%) as compared to the O from NiO (17%). Formation of surface layer of Al_2O_3 in Alloy 693 is also observed when the alloy is subjected to high temperature borosilicate melt [23] or oxidizing environment [27] for providing diffusion barrier coating. No iron was identified in the surface layer.

XRD measurements confirm that the oxide layer formed on Alloy 690 after exposure to FLiNaK salt is mainly Cr_2O_3 and NiO type (Fig. 8(a)). XPS analyses (Fig. 8), indicate that after exposure Cr existed mainly as Cr^{3+} and Cr^0 with its $2p_{3/2}$ binding energy peaks at 575.5 eV and 574.2 eV respectively. Ni was also observed to be in +2 state as well as the elemental state with its $2p_{3/2}$ peaks occurring respectively at 858.8 eV and 853.2 eV [11]. The deconvoluted O1s binding energy peaks occur at a 528.0 eV (corresponding

to oxide of Ni) and 530.0 eV (corresponding to oxide of Cr) indicating that the surface film comprises of oxides of Ni and Cr mainly of type Cr_2O_3 and NiO [11,27]. Furthermore, from the area percentage of the deconvoluted O peaks, it is evident that contribution to O 1s peak from the oxygen in Cr_2O_3 is higher (83.6%) as compared to the O from NiO (16.4%). No iron was identified in the surface layer. Presence of metallic state of Ni and Cr suggest that these oxides are either porous or dis-continuous exposing metallic islands at places.

Table 3 summarizes the results for different alloys obtained from XRD and XPS techniques. No Fluorine is detected in XPS measurements which is expected since the excess fluorides on the alloy surface were cleaned using acetone.

4. Discussion

From the analyses of surface films and microstructure of the alloys, a reaction mechanism is proposed for the alloy corrosion. In absence of oxygen, the corrosion occurs via dissolution of alloy elements into salt and penetration of F. The electrochemical corrosion reaction between alloy and molten salt [2,28] is as follows:

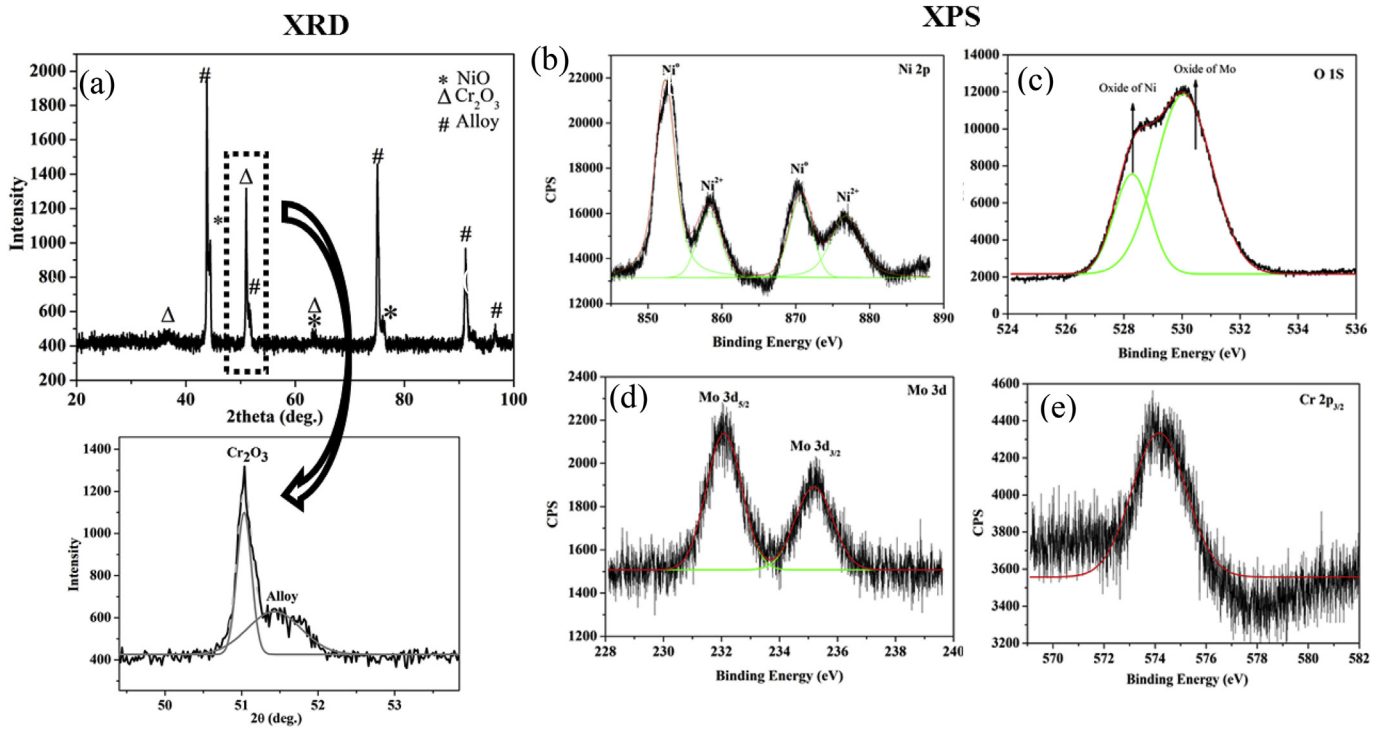


Fig. 6. (a) XRD pattern and (b)–(e) High resolution XPS spectra for Ni 2p, O 1s, Mo 3d and Cr 2p_{3/2} peaks corresponding to exposed Ni-Mo-Cr alloy surface.

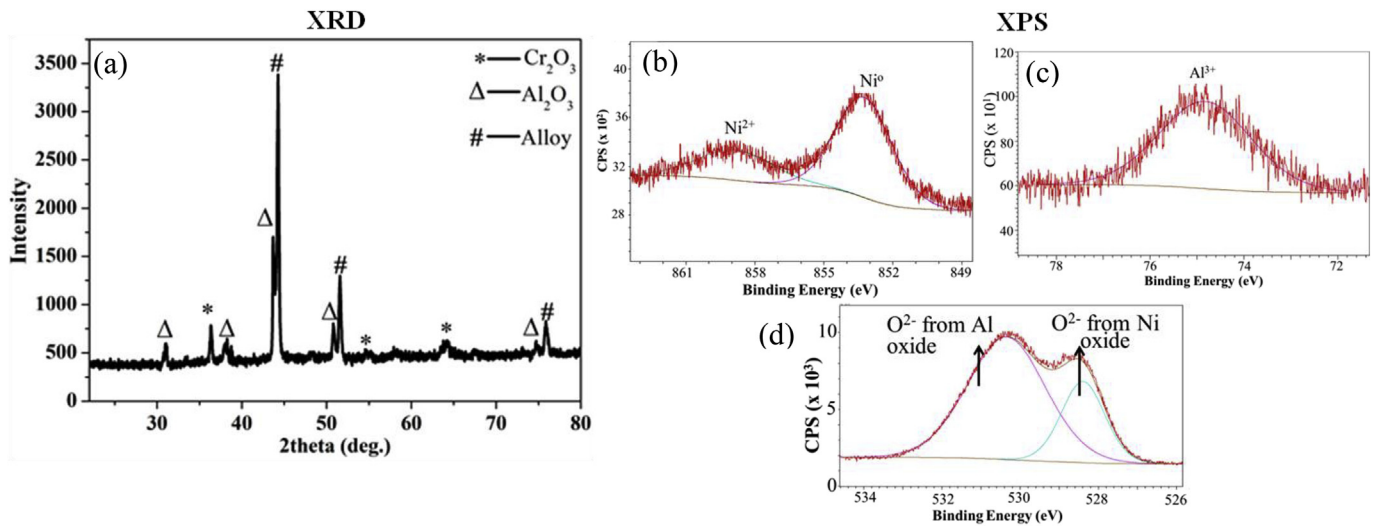


Fig. 7. (a) XRD pattern and high resolution XPS spectra for (b) Ni 2p_{3/2}, (c) Al 2p, (d) Cr 2p_{3/2} and (e) O 1s for exposed Alloy 693 surface.

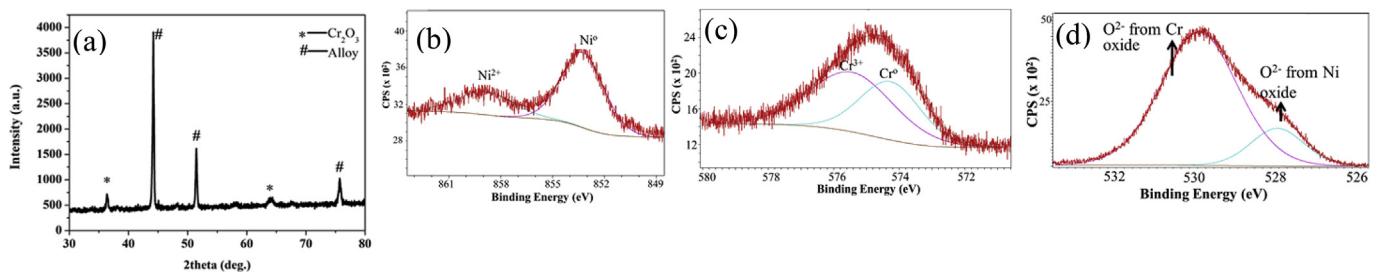


Fig. 8. (a) XRD pattern and (b)–(d) High resolution XPS spectra for (a) Ni 2p_{3/2}, (b) Cr 2p_{3/2} and (c) O 1s for exposed Alloy 690 surface.

Table 3
Oxide layer formed on Ni-based alloys identified by XRD and XPS.

Alloy	XRD	XPS	Possible configuration
Alloy 690	Cr ₂ O ₃	NiO, Cr ₂ O ₃	<div style="border: 1px solid black; padding: 2px; margin-bottom: 2px;">NiO</div> <div style="border: 1px solid black; padding: 2px; margin-bottom: 2px;">Cr₂O₃</div> <div style="border: 1px solid black; padding: 2px;">Alloy</div>
Alloy 693	Al ₂ O ₃ , Cr ₂ O ₃	NiO, Al ₂ O ₃	<div style="border: 1px solid black; padding: 2px; margin-bottom: 2px;">NiO</div> <div style="border: 1px solid black; padding: 2px; margin-bottom: 2px;">Al₂O₃</div> <div style="border: 1px solid black; padding: 2px; margin-bottom: 2px;">Cr₂O₃</div> <div style="border: 1px solid black; padding: 2px;">Alloy</div>
Alloy Ni-Mo-Cr	NiO, Cr ₂ O ₃	NiO, MoO ₃	<div style="border: 1px solid black; padding: 2px; margin-bottom: 2px;">MoO₃</div> <div style="border: 1px solid black; padding: 2px; margin-bottom: 2px;">NiO</div> <div style="border: 1px solid black; padding: 2px; margin-bottom: 2px;">Cr₂O₃</div> <div style="border: 1px solid black; padding: 2px;">Alloy</div>



However in presence of oxygen, there is a competitive diffusion of F and O in the alloys. The activation energy for diffusion and diffusion coefficient at 973 K for F is 118.6 kJ/mol and $\sim 4.03 \times 10^{-9} \text{ cm}^2/\text{s}$ [29] respectively while the values are respectively 182.0 kJ/mol and $\sim 0.94 \times 10^{-9} \text{ cm}^2/\text{s}$ for O [30]. Hence both oxygen and fluorine (from molten salt, HF) penetrate the alloy surface resulting in the formation of oxide patches along with the formation of fluorides. The Gibbs free energy for fluoride formation of various Ni, Al, Cr and Mo fluorides follows the trend $\text{AlF}_3 < \text{CrF}_2 < \text{CrF}_3 < \text{NiF}_2 < \text{MoF}_2$ [2] and thus mainly Cr rich fluorides are formed at the surface which dissolve into the molten salt. For example, the solubility of CrF_3 in FLiNaK salt at 700 °C is reported to be 0.96 wt% [31]. Thus dissolution of Cr rich fluorides - sets up a concentration gradient of Cr between the alloy matrix and surface resulting in more Cr diffusion. Similar mechanism was proposed for depletion of Cr in Cr_{23}C_6 type carbides at high angle boundaries by Dai et al. [25]. The mechanism of interaction is depicted schematically in Fig. 9.

The diffusivity of Cr in all the three alloys in presence of FLiNaK salt, is estimated from the Cr depletion depth (from SEM) using relation [25].

$$x = (2D_{\text{eff}}t)^{1/2} \quad (3)$$

where x is the depth of Cr depletion known as characteristic diffusion distance and t is the exposure time.

The calculated diffusion coefficients for Cr are observed to follow the trend $D_{690} > D_{693} > D_{\text{Ni-Mo-Cr}}$ (Table 4). In presence of FLiNaK salt, diffusivity of Cr is increased atleast by two orders as compared to diffusion of Cr in pure Ni ($D_{\text{Cr/Ni}}$) without salt [32]. On the other hand the diffusivity of Cr^{2+} ion in molten salt ($D_{\text{Cr}^{2+}/\text{FLiNaK}}$) is reported to be $2.9 \pm 0.8 \times 10^{-10} \text{ m}^2\text{sec}^{-1}$ at 700 °C [25,33]. The oxide layers formed on the alloy surfaces are ineffective in mitigating the diffusion of Cr. In fact Cr diffusivity from alloy matrix to surface was found to increase with Cr concentration. In case of Ni-Mo-Cr alloy, the Cr diffusivity is higher when oxygen is present in molten salt as compared to the case where the salt is free from oxygen [15]. The increase in Cr diffusivity in presence of oxygen layer is attributable to the formation of galvanic micro-cell between oxide layer (more noble) and exposed alloy surface [34]. The exposed surface now becomes more active than the oxide layer and a higher concentration gradient of Cr between alloy matrix and alloy surface is set up as compared to the case where the molten salt is free from oxygen (Fig. 9).

The lower Cr depletion and Cr diffusivity in case of Ni-Mo-Cr alloy as compared to Alloy 690 and 693 can be attributed to the fact that MoO_3 layer formed over the areas devoid of oxide patches may prevent the formation of galvanic micro-cell between oxide and exposed surface or reduce galvanic coupling between Ni-, Cr-rich oxide and the exposed surface.

In order to predict Cr concentration profile under long term corrosive attack, solution of Fick's second law of diffusion having following form is used [13].

$$C_{\text{Cr}}(x, t) = C_{0,\text{Cr}}(x, t) \text{erf} \left(\frac{x}{2\sqrt{D_{\text{eff}}t}} \right) \quad (4)$$

where x is the distance from alloy surface (the oxide layer is not considered), D_{eff} is the effective diffusion coefficient of Cr in alloy under FLiNaK environment and t is the exposure time. Fig. 10 shows

Table 4

Estimated diffusion coefficients of Cr in Alloy 690, 693 and Ni-Mo-Cr alloy at 973 K under FLiNaK environment.

Alloy	$D_{\text{eff}} (\times 10^{-15} \text{ m}^2/\text{s})$	Error in estimation of $D_{\text{eff}} (\times 10^{-15} \text{ m}^2/\text{s})$
690	6.67	0.09
693	3.0	0.1
Ni-Mo-Cr alloy	1.67	0.06

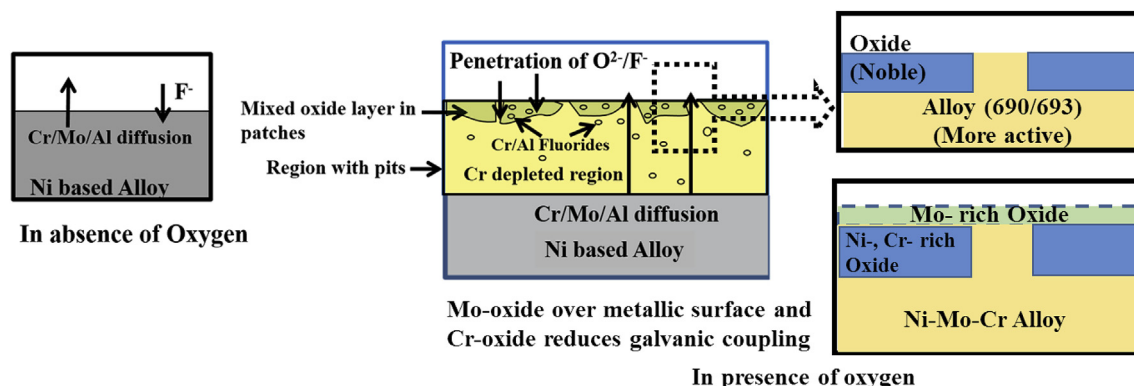


Fig. 9. Schematic representation of alloy corrosion in molten salt in (a) absence of oxygen and (b) presence of oxygen.

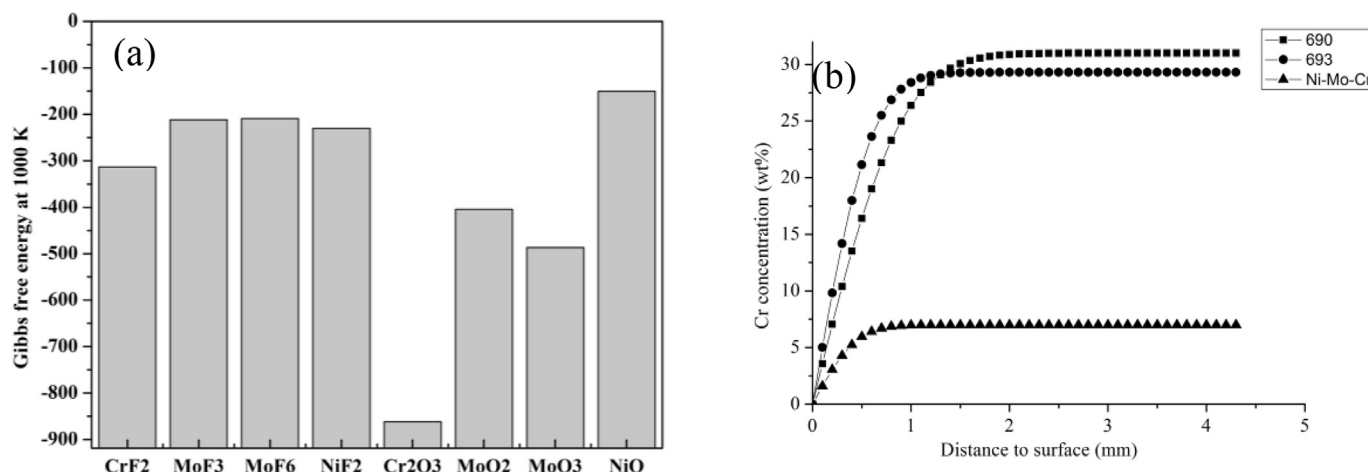


Fig. 10. (a) Gibbs free energy of various oxides and fluorides at 1000 K [2,14] and (b) Cr diffusion profile calculated for 10000 h exposure to FLiNaK salt.

the simulated Cr depletion profile after 10000 h of exposure for the three different alloys used in present study. Alloy 690 shows the highest depth of Cr depletion followed by Alloy 693 and Ni-Mo-Cr alloy. The calculated Cr diffusion profile for Ni-Mo-Cr alloy matches well with the profile for Hastelloy N calculated from the diffusion coefficients reported by Ye et al. [28].

The observations suggest that for use in reactor environments strict redox control and purification of alloys is needed as diffusivity of elements are high enhanced in fluoride melt. The oxide layers developed are partially protective and also do not mitigate the internal penetration of F.

5. Summary

Ni-based alloys viz. Alloy 690, Alloy 693 and Ni-17 wt.% Mo-7wt.% Cr were exposed to eutectic LiF-NaF-KF melt at 973 K in presence of oxygen Alloy 690 formed a mixed oxide comprising NiO and Cr₂O₃ while Alloy 693 surface developed NiO and Al₂O₃ followed by a layer of Cr₂O₃. In case of Ni-17 wt.% Mo-7wt.% Cr alloy oxides of MoO₃ and NiO type were formed followed by a layer of Cr₂O₃. Based on W_{Fe+Cr} index the corrosion in the alloys as well as Cr diffusivity followed the trend Alloy 690 > Alloy 693 > Ni-Cr-Mo alloy suggesting that increase in Cr concentration increased the depth of Cr depletion and fluoride attack. The oxide layers are only partially protective as there is formation of galvanic micro-couple between oxide and exposed surface which causes the exposed alloy surface more prone to attack. The lower Cr depletion in case of Ni-Mo-Cr alloy as compared to Alloy 690 and 693 can be attributed to the fact that MoO₃ layer present on the exposed alloy surface may prevent/reduce galvanic coupling between Ni-,Cr-rich oxides and exposed surface.

Data availability statement

The raw/processed data required to reproduce these findings cannot be shared at this time as the data also forms part of an ongoing study.

Acknowledgements

Present study was funded by Department of Atomic Energy, Government of India. The authors are thankful to Dr. Naveen Kumar, Materials Science Division for helping with SEM characterization. The authors also thank Dr. Madangopal, Associate

Director, Materials Group and Dr. R. S. Dutta, Materials Science Division for their keen interest in the work.

References

- [1] S. Delpach, C. Cabet, C. Slim, G.S. Picard, Molten fluorides for nuclear applications, *Mater. Today* 13 (2010) 34–41.
- [2] L.C. Olson, J.W. Ambrosek, K. Sridharan, M.H. Anderson, T.R. Allen, Materials corrosion in molten LiF–NaF–KF salt, *J. Fluorine Chem.* 130 (2009) 67–73.
- [3] C. W. Forsberg, P. F. Peterson, H. Zhao, High-temperature liquid-fluoride-salt closed-Brayton-cycle solar power towers, *J. Sol. Energy Eng.* 129 (2) 141–146. doi:10.1115/1.2710245.
- [4] V. Khokhlov, V. Ignatiev, V. Afonichkin, Evaluating physical properties of molten salt reactor fluoride mixtures, *J. Fluorine Chem.* 139 (2009) 30–37.
- [5] C. Le Brun, Molten salts and nuclear energy production, *J. Nucl. Mater.* 360 (2007) 1–5.
- [6] J. Hou, G. Yu, C. Zeng, H. Ai, R. Xie, Y. Chen, X. Zhou, L. Xie, J. Wang, Effects of exposing duration on corrosion performance in weld joint of Ni-Mo-Cr alloy in FLiNaK molten salt, *J. Fluorine Chem.* 191 (2016) 110–119.
- [7] D.F. Williams, L. Toth, K. Clarno, ORNL/TM-2006/12, 2006, pp. 1–69.
- [8] F. Ouyang, C. Chang, B. You, T. Yeh, J. Kai, Effect of moisture on corrosion of Ni-based alloys in molten alkali fluoride FLiNaK salt environments, *J. Nucl. Mater.* 437 (2013) 201–207.
- [9] A.F. Rowcliffe, L.K. Mansur, D.T. Hoelzer, Perspectives on radiation effects in nickel-base alloys for applications in advanced reactors, *J. Nucl. Mater.* 392 (2009) 341–352.
- [10] K.L. Murty, I. Charit, Structural materials for Gen-IV nuclear reactors: challenges and opportunities, *J. Nucl. Mater.* 383 (2008) 189–195.
- [11] R.S. Dutta, C. Yusufali, B. Paul, S. Majumdar, P. Sengupta, R.K. Mishra, C.P. Kaushik, R.J. Kshirsagar, U.D. Kulkarni, G.K. Dey, Formation of diffusion barrier coating on superalloy 690 substrate and its stability in borosilicate melt at elevated temperature, *J. Nucl. Mater.* 432 (2013) 72–77.
- [12] Y. Wang, H. Liu, G. Yu, J. Hou, C. Zeng, Electrochemical study of the corrosion of a Ni-based alloy GH3535 in molten (Li,Na,K)F at 700 °C, *J. Fluorine Chem.* 178 (2015) 14–22.
- [13] R.S. Sellers, M.H. Anderson, K. Sridharan, T.R. Allen, Failure analysis of 316L stainless steel crucible by molten fluoride salt interaction with clay bonded silicon carbide, *Eng. Fail. Anal.* 42 (2014) 38–44.
- [14] G. Zheng, L. He, D. Carpenter, K. Sridharan, Corrosion-induced microstructural developments in 316 stainless steel during exposure to molten Li₂BeF₄ (FLiBe) salt, *J. Nucl. Mater.* 482 (2016) 147–155.
- [15] F. Ouyang, C. Chang, J. Kai, Long-term corrosion behaviors of Hastelloy-N and Hastelloy-B3 in moisture-containing molten FLiNaK salt environments, *J. Nucl. Mater.* 446 (2014) 81–89.
- [16] R. Fujimura, M. Yamawaki, Y. Arita, Corrosion behavior of Hastelloy-N alloys in molten salt fluoride in Ar gas or in air, Kenichi Fukumoto, *J. Nucl. Sci. Technol.* 52 (2015) 1323–1327. <https://doi.org/10.1080/00223131.2015.1043155>.
- [17] V. Pavlik, M. Kontrik, M. Boča, Corrosion behavior of Incoloy 800H/HT in the fluoride molten salt FLiNaK + MF_x (MF_x = CrF₃, FeF₂, FeF₃ and NiF₂), *New J. Chem.* 39 (2015) 9841–9847.
- [18] P. Sengupta, C.P. Kaushik, G.B. Kale, D. Das, K. Raj, B.P. Sharma, Evaluation of alloy 690 process pot at the contact with borosilicate melt pool during vitrification of high-level nuclear waste, *J. Nucl. Mater.* 392 (2009) 379–385.
- [19] R. Halder, R.S. Dutta, P. Sengupta, I. Samajdar, G.K. Dey, Microstructural studies on alloy 693, *J. Nucl. Mater.* 453 (2014) 91–97.
- [20] R.S. Dutta, R. Tewari, Microstructural and corrosion aspects of alloy 690, *Br.*

- Corros. J. 34 (1999) 201–205.
- [21] S. Khan, J.B. Singh, A. Verma, Age hardening behaviour of alloy 693, *Mat. Sci. Eng. A* 697 (2017) 86–94. <https://doi.org/10.1016/j.msea.2017.04.109>.
- [22] H. Zhu, B. Li, M. Chen, Z. Liu, Z. Tang, C. Qiu, AlN coatings on Hastelloy-N alloy offering superior corrosion resistance in LiF-KF-NaF molten salt, *J. Fluorine Chem.* 213 (2018) 80–86.
- [23] R. Halder, P. Sengupta, Geogy Abraham, C.P. Kaushik, G.K. Dey, Interaction of Alloy 693 with borosilicate glass at high temperature; *Mater. Today: Proceedings* 3 (2016) 3025–3034.
- [24] J. Qiu, Y. Zou, G. Yu, H. Liu, Y. Jia, Z. Li, P. Huai, X. Zhou, H. Xu, Compatibility of container materials with Cr in molten FLiNaK salt, *J. Fluorine Chem.* 168 (2014) 69–74.
- [25] Q. Dai, X. Xi Ye, H. Ai, S. Chen, L. Jiang, J. Liang, K. Yu, B. Leng, Z. Li, X. Zhou, Corrosion of Incoloy 800H alloys with nickel cladding in FLiNaK salts at 850 °C, *Cor. Sci.* 133 (2018) 349–357. <https://doi.org/10.1016/j.corsci.2018.01.026>.
- [26] A. Ul-Hamid, A.I. Mohammed, S.S. Al-Jaroudi, H.M. Tawancy, N.M. Abbas, Evolution of oxide scale on a Ni-Mo-Cr alloy at 900 °C, *Mater. Char.* 58 (1) (2007) 13–23.
- [27] R.S. Dutta, Rumu H. anerjee, G.K. Dey, An XPS study with depth profiling for the surface oxide layer formed on aluminides produced on superalloy 690 substrates, *Oxid. Metals* 89 (2018) 699–711.
- [28] X. Ye, H. Ai, Z. Guo, H. Huang, L. Jiang, J. Wang, Z. Li, X. Zhou, The high temperature corrosion of Hastelloy N alloy (UNS N 10003) in molten fluoride salts analysed by STXM, XAS, XRD, SEM, EPMA, TEM/EDS, *Corros. Sci.* 106 (2016) 249–259.
- [29] S. Garruchet, O. Politano, P. Arnoux, V. Vignal, Diffusion of oxygen in nickel: a variable charge molecular dynamics study, *Solid State Commun.* 150 (2010) 439–442.
- [30] L. Olson, K. Sridharan, M. Anderson, T. Allen, Nickel plating for active metal dissolution resistance in molten fluoride salts, *J. Nucl. Mater.* 411 (2013) 51–59.
- [31] H. Yin, P. Zhang, X. An, J. Cheng, X. Li, S. Wu, X. Wu, W. Liu, L. Xie, Thermodynamic modeling of LiF-NaF-KF-CrF₃ system, *J. Fluorine Chem.* 209 (2018) 6–13.
- [32] S.N.S. Redday, R.A. Rapp, The diffusivity and solubility of fluorine in solid nickel from electrochemical measurements, *Metall. Trans. B* 11 (1980) 99–106, <https://doi.org/10.1007/BF02657178>.
- [33] D.E. Holcomb, G. Muralidharan, D.F. Wilson, High Strength Alloys for High Temperature Service in Liquid-Salt Cooled Energy Systems, United States Patent Publication, 2017. US9540714 B2.
- [34] Y. Wang, S. Zhang, X. Ji, P. Wang, W. Li, Material corrosion in molten fluoride salts, *Int. J. Electrochem. Sci.* 13 (2018) 4891–4900, <https://doi.org/10.20964/2018.05.33>.